Master's Thesis

Nano-Structured Cathode for Improving Performance of Solid Oxide Fuel Cells

Seungtae Lee

Department of Energy Engineering

(Energy Engineering)

Graduate School of UNIST

2020

Nano-Structured Cathode for Improving Performance of Solid Oxide Fuel Cells

Seungtae Lee

Department of Energy Engineering
(Energy Engineering)

Graduate School of UNIST

Nano-Structured Cathode for Improving Performance of Solid Oxide Fuel Cells

A thesis
submitted to the Graduate School of UNIST
in partial fulfillment of the
requirements for the degree of
Master of Science

Seungtae Lee

11/18/2019
Approved by

Advisor
Guntae Kim

Nano-Structured Cathode for Improving Performance of Solid Oxide Fuel Cells

Seungtae Lee

This certifies that the thesis of Seungtae Lee is approved.

11/18/2019

signature

Advisor: Guntae Kim

signature

Changhee Sohn

signature

Ikwhang Chang

Abstract

Solid oxide fuel cells (SOFCs) are recognized as next-generation environmentally friendly energy conversion devices due to their high energy conversion efficiency, fuel flexibility, efficient reclamation of waste heat, and low pollutant emissions. Nevertheless, the commercialization of SOFCs has been impeded by reason of some issues associated with the high operating temperatures (800-1000ºC) such as undesired reactions between cell components, high cost, and material compatibility challenges. Thus, reducing the operating temperatures toward an intermediate-temperature range (600-800ºC) is essential to overcome the aforementioned problems. In intermediate-temperature SOFCs (IT-SOFCs), however, electrocatalytic activity toward oxygen reduction reaction at the cathode is significantly decreased, which in turn causes insufficient fuel cell performance. Current researches, therefore, have been focused on enhancing the performance of cathode for effective IT-SOFC operation.

In this regard, the infiltration method could be an excellent cathode fabrication method, considering its outstanding advantages toward intermediate temperature operation. First, each optimized sintering temperature of cathode and electrolyte can be applied, ensuring the favorable characteristics for IT-SOFC operation. Second, due to relatively low sintering temperature, nano-structured cathodes can be formed, resulting in enlarged surface area and enhancement of electrochemical performance. Finally, long-term stability is improved because the thermal expansion coefficient between cathode and electrolyte is minimized.

This thesis mainly focuses on the fabrication of SOFC cathode by the infiltration method to achieve high fuel cell performance in the intermediate temperature range. Herein, my research paper studying infiltrated cathode materials for IT-SOFC is presented as follows.

- A Nano-structured SOFC Composite Cathode Prepared via Infiltration of $La_{0.5}Ba_{0.25}Sr_{0.25}Co_{0.8}Fe_{0.2}O_{3-\delta}$ into $La_{0.9}Sr_{0.1}Ga_{0.8}Mg_{0.2}O_{3-\delta}$ for Extended Triple- Phase Boundary Area

Contents

List of Figures

List of Tables

Chapter 1. Introduction

1.1 Motivation and Research Objective

In recent decades, most of the energy supplies have relied on fossil fuels such as coal, oil and natural gas. The chemical energy of fossil fuels is converted into electrical energy through the combustion process. In fossil fuel combustion, hydrocarbon dioxide reacts with oxygen, and carbon dioxide, steam, and heat are produced. As the worldwide population and energy demand increase, the amount of atmospheric carbon dioxide increases, accelerating global warming. To overcome this environmental issue and finite fossil fuel supplies problem, the environmental-friendly energy storage and conversion devices need to be developed.

In these regards, solid oxide cells (SOCs) have attracted great attention as next-generation renewable energy conversion devices because of their high efficiency, fuel flexibility, and low pollutant emissions. SOCs can operate in two ways: fuel cell and electrolysis mode. In the fuel cell mode, the chemical energy of fuels is directly converted into electrical energy. In the electrolysis mode, electricity is used to produce fuels such as hydrogen and synthetic fuels. Generally, conventional SOCs operate in the temperature range of 800^{o}C to 1000^{o}C. These high operating temperatures, however, cause serious commercialization challenges including high degradation rates, materials cost issues, and material compatibility problems. To avoid those problems related to the high-temperature operation, the operating temperature of SOCs should be reduced down to an intermediate temperature range (600-800^{o}C). Unfortunately, the electrocatalytic activity of electrode materials is decreased in the intermediate temperature range, resulting in insufficient fuel cell performance. Especially, the oxygen reduction reaction activities at the cathode should be enhanced for the excellent cell performances. In this regard, the infiltration method could be an excellent cathode fabrication method due to its outstanding advantages. Therefore, my research focuses on the fabrication of solid oxide fuel cell cathode by an infiltration method in order to achieve high cell performance in the intermediate temperature range.

1.2 General Introduction of Solid Oxide Fuel Cell (SOFC)

1.2.1 Basic of Fuel Cell

With global energy and environmental concerns growing, many researchers have been widely studying clean and renewable energy devices. Fuel cells are the most attractive energy devices to solve worldwide energy and environmental issues because, in theory, they can produce unlimited electricity by supplying fuel infinitely. Also, fuel cells directly convert the chemical energy of fuels into electrical energy, which has higher energy conversion efficiency than combustion engines. Hydrogen fuel cells, a typical type of fuel cells, are environmentally friendly because the product of the chemical reaction is only water and heat. Hydrogen fuel cells produce electrical energy through electrochemical reactions at two opposite sites as follows:

$$H_2 \leftrightarrow 2H^+ + 2e^- \tag{1.1}$$

$$\frac{1}{2}O_2 + 2H^+ + 2e^- \leftrightarrow H_2O \tag{1.2}$$

$$H_2 + \frac{1}{2}O_2 \leftrightarrow H_2O \tag{1.3}$$

In hydrogen fuel cells, the hydrogen oxidation reaction takes place at the anode as shown in equation 1.1, while the oxygen reduction reaction occurs at the cathode as shown in equation 1.2. Hydrogen ions move from the anode to the cathode through the electrolyte, and electrons are transferred by an external circuit. Considering that the reaction product is only water, as can be seen in equation 1.3, the fuel cell will be an outstanding solution to future energy and environmental problems if hydrogen is supplied by eco-friendly way continuously. Fuel cells can be categorized according to the type of electrolyte and operating temperature as shown in Table 1.1.[1]

	Alkaline Fuel Cell (AFC)	Phosphoric Acid Fuel Cell (PAFC)	Polymer Electrolyte Membrane Fuel Cell (PEMFC)	Direct Methanol Fuel Cell (DMFC)	Molten Carbonate Fuel Cell (MCFC)	Solid Oxide Fuel Cell (SOFC)
Electrolyte	Alkali	Phosphoric acid	Polymer membrane	Polymer membrane	Molten carbonate	Ceramic
Operating temperature (°C)	50 - 200	150 - 200	50 - 100	50 - 110	600 - 700	600 - 1000
Mobile ion	OH^-	H^+	H^+	H^+	CO_3^{2-}	O^{2-}
Primary Fuel	Hydrogen	Hydrogen	Hydrogen	Methanol	Hydrogen, Methane	Hydrogen, Hydrocarbon fuel (CH_4, C_3H_8)

Table 1.1. Types of fuel cells according to their characteristics.

1.2.2 Basic Operating Principle of SOFC

Solid oxide fuel cells (SOFCs) directly convert the chemical energy of fuel into electrical energy without Carnot-cycle efficiency restriction. As can be seen in Figure 1.1, SOFCs consist of cathode, anode, and electrolyte. The cathode must withstand the highly oxidizing condition in high-temperature operation, while the anode must endure the highly reducing environment in high-temperature operation.[2] Also, each electrode should have a porous structure for smooth gas diffusion. At the cathode, oxygen ions are produced by the oxygen reduction reaction (ORR) as shown in equation 1.4.

$$O_2 + 4e^- \rightarrow 2O^{2-} \tag{1.4}$$

These oxygen ions pass through the dense ceramic electrolyte. Then, hydrogen oxidation reaction (HOR) occurs by combining hydrogen with oxygen ions at the anode, producing water and electrons as shown in equation 1.5.

$$2H_2 + 2O^{2-} \rightarrow 2H_2O + 4e^- \tag{1.5}$$

These electrochemical reactions, ORR and HOR, occur at the triple-phase boundary (TPB) area where the gas phase, electronic phase, and ionic phase come into contact with each other.

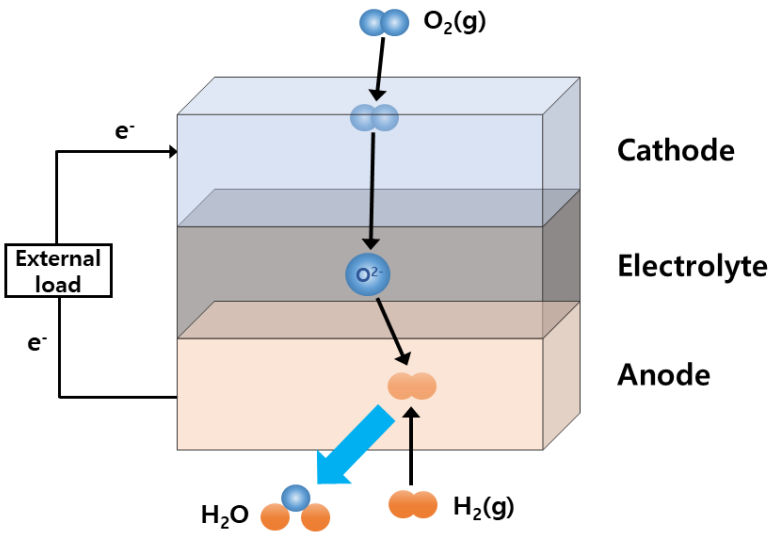

Figure 1.1. Schematic of solid oxide fuel cell operation.

1.2.3 Advantages and Challenges of SOFC

SOFCs generally adopt solid oxide-based electrode and electrolyte materials and operate at high temperatures (800-1000°C). Conventional SOFCs have much higher energy conversion efficiency than combustion engines because they directly convert the chemical energy of fuel into electrical energy. Moreover, it can be possible to improve efficiency by utilizing high-quality waste heat. Since the hydrocarbon fuel can be used directly without external reforming process, SOFCs have flexibility and convenience for fuel use. Finally, SOFCs are environmentally-friendly devices because it can reduce emissions of air pollutants such as CO_2, NO_x, and SO_x if hydrogen is used as a fuel. Nevertheless, the commercialization of SOFCs has been impeded by some issues derived from a high-temperature operation such as material durability issues, cost competitiveness, sealing and interconnect problems, and thermal stress between cell component.[2] Hence, researches are being actively conducted to lower the operating temperature to the intermediate-range (600-800°C).[3-5] Intermediate temperature solid oxide fuel cell (IT-SOFC) can alleviate the drawbacks of high-temperature operation while retaining the advantages of conventional SOFC. However, it is essential to develop materials that maintain high electrocatalytic activity and stability even in the intermediate temperature range, since lower operating temperatures reduce the electrocatalytic activity of the electrode material and the ionic conductivity of the electrolyte.

1.3 Theoretical Background

1.3.1 Fundamental Thermodynamics of SOFC

In SOFC, the Gibbs free energy of the combustion reaction of a fuel and an oxidant is directly converted into electrical energy. A reversible fuel cell is governed by the first and the second law of thermodynamics. Equation 1.6 shows the first law of thermodynamics.[6]

$$q + w = \Delta H \tag{1.6}$$

The molar reaction enthalpy (ΔH) of the oxidation is comprised of work and heat energy. The second law of thermodynamics governs the reversibility of the transport process and is applied to reversible processes as following equation 1.7

$$\oint dS = 0 \;\rightarrow\; q = q_{rev} = T\Delta S \tag{1.7}$$

We can redescribe as equation 1.8 because the reversible heat exchange with the environment equalizes the generated reaction entropy,

$$q_{rev} + w_{rev} = \Delta H \tag{1.8}$$

The reaction entropy (ΔS) is a result of the different opportunities of the species to save thermal energy between the absolute zero level of temperature and the temperature level of the reactor. Combining equation 1.4 and equation 1.5, we can derive molar reversible work (w_{rev}),

$$w_{rev} = \Delta H \; - \; T\Delta S \tag{1.9}$$

The reversible work of the reaction is identical with the Gibbs free energy of the reaction with the ambient temperature as a reference for the calculation of the Gibbs free energy.

$$w_{rev} = \Delta G = \Delta H \; - \; T\Delta S \tag{1.10}$$

Thermodynamic potentials can be utilized to identify the energy transfer from one form to another on the basis of the first and second law of thermodynamics. Using the first and second law of

thermodynamics, internal energy can be described by the variation of two independent variables of entropy (S) and volume (V) where p is the pressure and T is the temperature.[7]

$$dU = TdS - pdV \tag{1.11}$$

In equation 1.11, TdS is the reversible heat transfer and pdV is the mechanical work. The following equations present how the dependent variables (T and p) are related to variations in the independent variables (S and V):

$$(\frac{dU}{dS})_V = T \tag{1.12}$$

$$(\frac{dU}{dV})_S = -p \tag{1.13}$$

U can be rewritten by a Legendre transform with defining the new thermodynamic potential G (T, p) as follows:

$$G = U - (\frac{dU}{dS})_V S - (\frac{dU}{dV})_S V \tag{1.14}$$

From equation 1.12 and 1.13, equation 1.15 can be obtained as follows:

$$G = U - TS + pV \tag{1.15}$$

The variation of G results in

$$dG = dU - TdS - SdT + pdV + Vdp \tag{1.16}$$

From equation 1.11, we obtain

$$dG = -SdT + Vdp \tag{1.17}$$

The new thermodynamic potential (H) is defined as follows:

$$H = U - (\frac{dU}{dV})_S V \tag{1.18}$$

According to equation 1.13, equation 1.18 can be transformed into as follows:

$$H = U + pV \tag{1.19}$$

where H designates enthalpy. Using differentiation, H can be defined by a function of S and p.

$$dH = dU + pdV + Vdp \tag{1.20}$$

$$dH = TdS + Vdp \tag{1.21}$$

The difference of Gibbs free energy of formation for the overall reaction of SOFC can be presented as follows:

$$\Delta G = \Delta G_{H_2O} - \Delta G_{H_2} - \frac{1}{2}\Delta G_{O_2} \tag{1.22}$$

Assume all the Gibbs free energy is consumed to electrical work, then

$$\Delta G = -nFE \tag{1.23}$$

where n, F, and E indicate the number of electrons involved in the chemical reaction, the Faraday constant, and the reversible potential, respectively. The reversible standard potential (E^0) of the electrochemical reaction can be defined as equation 1.24 if the reactants and products are all in their standard states,

$$E^0 = -\frac{\Delta G^0}{nF} \tag{1.24}$$

The standard electrode potential can be calculated by substituting the standard state values (T = 273.15 K, p = 1 atm) into equation 1.24.

$$E^0 = \frac{2379000\ J\ mol^{-1}}{2\times 96485\ C\ mol^{-1}} = 1.23\ \text{V} \tag{1.25}$$

The theoretical reversible potential (E_{th}) is derived by the Nernst equation,

$$E_{th} = E^0 - \left(\frac{RT}{2F}\right)\ln\left(\frac{P_{H_2O}}{P_{H_2}P_{O_2}^{\frac{1}{2}}}\right) \tag{1.26}$$

where R is the gas constant, T is the absolute temperature, and p is the partial pressure of each gas.

1.3.2 Performance of SOFC

The performance of SOFC can be described with a current-voltage (*i*-*V*) curve. The current-voltage curves display the output voltage of the SOFC for a given current density. In practice, the real SOFCs deliver less power than ideal SOFCs due to several polarization losses.[2] The power output can be calculated as the product of current and voltage.

$$P = iV \tag{1.27}$$

The ideal and real SOFC *i*-*V* characteristics are shown in Figure 1.2.

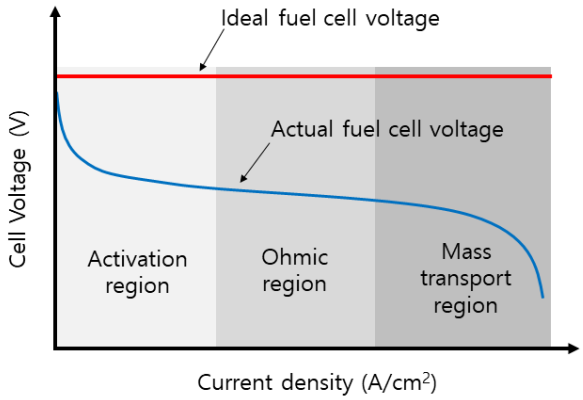

Figure 1.2. Schematic of fuel cell *i*-*V* curve.

The polarization losses, also known as overpotential (η), cause the difference between thermodynamically predicted fuel cell voltage and actual fuel cell voltage. The real cell voltage can be written as equation 1.28,

$$V = E_{thermo} - \eta_{act} - \eta_{ohmic} - \eta_{conc} \tag{1.28}$$

The polarization losses are composed of activation polarization which is in charge of the initial part of the voltage curve, ohmic polarization which is in charge of the slow voltage drop in the middle region of the voltage curve, and concentration polarization responsible for the end section of the voltage curve. These polarization losses will be explained in detail as follows:

Activation Polarization

Activation polarization is related to the reaction kinetics. To overcome the activation barrier, partial loss of the voltage should be entailed to enhance the reaction rate. This voltage loss is named as activation polarization. The relationship between the current density and the activation polarization can be described by the Butler-Volmer equation as

$$j = j_0 \left[e^{\frac{\alpha n F \eta_{act}}{RT}} - e^{-\frac{(1-\alpha) n F \eta_{act}}{RT}} \right] \tag{1.29}$$

where j is the current density, j_0 is the exchange current density, α is the charge transfer coefficient, and η is the activation polarization. The Butler-Volmer equation states that voltage loss will be higher if we want to get more electricity from the fuel cell.

Ohmic Polarization

The inevitable voltage loss occurs during the charge transport process due to intrinsic resistance of a conductor. We call it as ohmic polarization (η_{ohmic}) because it obeys Ohm`s law.

$$\eta_{ohmic} = iR_{ohmic} = i(R_{elec} + R_{ionic}) \tag{1.30}$$

where R_{elec} and R_{ionic} indicate the electronic contribution and the ionic contribution to fuel cell resistance, respectively. Ohmic polarization losses can be minimized by reducing the thickness and increasing the conductivity of the electrolyte.

Concentration Polarization

Fuel cell mass transport contains the process of supplying reactants and removing products. The poor mass transport, however, leads to fuel cell performance degradation. This loss in performance is described as concentration polarization. The general form of the concentration polarization can be generalized as the following equation.

$$\eta_{conc} = c \, ln \frac{j_L}{j_L - j} \tag{1.31}$$

where c is a constant that relies on the geometry and mass transport properties of the fuel cell and j_L is the limiting current density.

1.3.3 Electrochemical Reaction Mechanism in SOFC Cathode

In SOFC cathode, oxygen reduction reaction (ORR) occurs through the following electrochemical reaction

$$O_{2,gas} + 2V_O^{\cdot\cdot} + 4e' \rightarrow 2O_O^x \quad (1.32)$$

where $V_O^{\cdot\cdot}$ is a vacant oxygen site, and O_O^x is an oxygen ion on a regular oxygen site in the electrolyte lattice. This reduction mechanism contains several basic electrochemical steps including adsorption, dissociation, surface diffusion, and charge transfer.[8] The ORR reaction occurs at the electrochemically reactive site where ionic conducting phase, electronic conducting phase and gas are in contact with each other. This reaction site is called the triple-phase boundary (TPB) site. The simple schematic illustration of the ORR mechanism and TPB site is presented in Figure 1.3.

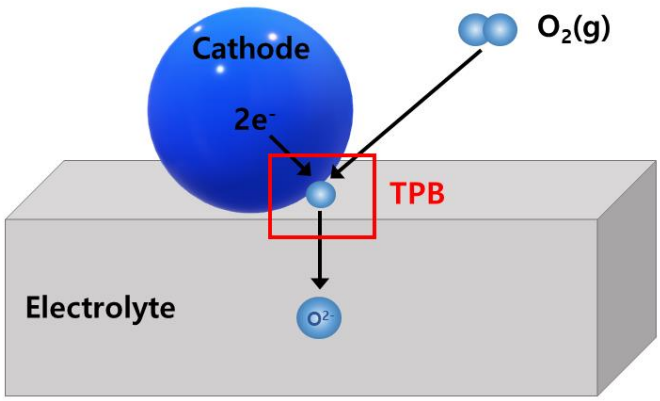

Figure 1.3. Schematic illustration of the triple-phase boundary (TPB) concept in SOFC cathode.

For more details, Adler et al. outlines a continuum model of the ORR mechanism at a mixed ionic-electronic conductor (MIEC)/electrolyte interface.[9] In this model, the oxygen molecule is chemically reduced to oxygen ion at the MIEC/gas interface. Then oxygen ion moves through the MIEC by solid-state diffusion. The chemical exchange of oxygen at the MIEC/gas interface was regarded as a non-charge transfer process. Figure 1.4 illustrates the simplified mechanisms of oxygen reduction at the

cathode.

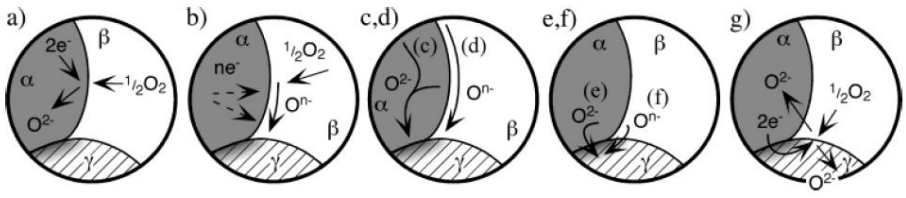

Figure 1.4. Some mechanisms thought to govern oxygen reduction in SOFC cathodes. Phases α, β, and γ refer to the electronic phase, gas phase, and ionic phase, respectively: (a) Incorporation of oxygen into the bulk of the electronic phase (if mixed conducting); (b) adsorption and/or partial reduction of oxygen on the surface of the electronic phase; (c) bulk or (d) surface transport of O^{2-} or O^{n-}, respectively, to the α/γ interface, (e) Electrochemical charge transfer of O^{2-} or (f) combinations of O^{n-} and e^-, respectively, across the α/γ interface, and (g) rates of one or more of these mechanisms wherein the electrolyte itself is active for generation and transport of electroactive oxygen species.[9]

1.3.4 Materials for SOFC Cathode

The general requirements for outstanding SOFC cathode materials are described as following.[10]

- High electrocatalytic activity for the ORR.
- Sufficient electronic conductivity
- Minimized thermal expansion coefficient mismatch between cathode and electrolyte.
- Long-term stability under operating conditions.
- Optimized microstructures for the overall reaction.

In this section, the characteristics of perovskite oxide and double perovskite oxide as cathode materials will be discussed.

1.3.4.1 Simple Perovskite Oxide

The ideal type of perovskite oxides (ABO_3) has a cubic structure. The A-site cations are larger than B-site cations and coordinate with twelve oxygen anions. The B-site cations are smaller than A-site cations and coordinate with six oxygen anions.[11] In this structure, rare-earth or alkaline-earth metal elements are used as A-site dopant and transition metal elements are used as B-site dopant. To determine the structural stability of perovskite oxides, the tolerance factor (t) can be used as a criterion for the deviation from the ideal cubic structure.[12] The tolerance factor can be described as the following equation,

$$t = \frac{(r_A + r_O)}{\sqrt{2}(r_B + r_O)} \tag{1.33}$$

where r_A, r_B, and r_O represent the ionic radius of A-site ion, B-site ion, and oxygen, respectively.
The perovskite-structured mixed ionic and electronic conductors (MIECs) have been extensively studied for SOFC cathode due to their excellent catalytic activity. Among them, cobalt-containing perovskite oxides such as $Ba_{0.5}Sr_{0.5}Co_{0.8}Fe_{0.2}O_{3-\delta}$, $La_{0.6}Sr_{0.4}Co_{0.2}Fe_{0.8}O_{3-\delta}$, and $Sm_{0.5}Sr_{0.5}CoO_3$ have attracted great attention as promising cathode materials.[13-16] Notwithstanding their attractive advantages, some drawbacks such as high cost of cobalt and TEC mismatch between electrolyte and electrode need to be solved.

1.3.4.2 Double Perovskite Oxide

The double perovskite oxides have the general formula of $AA'B_2O_{5+\delta}$, where A, A′ and B are trivalent lanthanide ion, alkaline earth metal, and first-row transition metal ion, respectively. In this structure, A and A′ cations are ordered along the c-direction. Double perovskite oxides have received wide attention due to their much higher oxygen ion diffusivity and a surface exchange coefficient than simple perovskite oxides.[17-18] Especially, $LnBaCo_2O_{5+\delta}$ (Ln = La, Pr, Nd, Sm, and Gd) compounds show fast oxygen kinetics and high mixed ionic and electronic conductivity.[3,18-22]

1.4 Advantages of Infiltration Method

It is necessary to develop superior electrode and electrolyte materials for outstanding SOFC performances. However, SOFC performances may vary depending on the electrode fabrication processes. Conventional electrode fabrication methods employ the deposition of electrode materials onto an electrolyte. For example, the deposited electrode composition can be electronic conductor alone, a mixture of electronic and ionic conductor, mixed ionic and ionic conductor (MIEC) alone, and MIEC with an ionic conductor. To ensure excellent performances with this method, each sintering temperature of electrolyte and electrode materials in the composite mixture should be carefully optimized. In this regard, the sintering temperature dilemma arises. The electrolyte materials in the composite mixture which act as ionic conducting phase require a high sintering temperature to ensure a good connection between the electrode and the electrolyte. On the other hand, the electrode materials which act as electronic conducting phase need to avoid too high sintering temperatures in order to prevent solid-state reactions with electrolyte materials in the composite and to obtain high performances.[23-25] Infiltration method can solve this dilemma and has additional advantages in electrode fabrication. First, it separates the sintering temperature of electrolyte and electrode, resulting in maximized respective functionalities. Various materials can be selected as an active phase due to reduced sintering temperature. Second, nano-structured electrodes can be established, providing a high surface area which is beneficial for gas diffusion and performance enhancement. Finally, thermal expansion coefficient (TEC) mismatch between electrolyte and electrode can be minimized. Based on these advantages, the infiltration method has attracted great attention as a promising electrode fabrication technique.

References

1. F. Alcaide, P. -L. Cabot, E. Brillas, *J. Power Sources* **2006**, *153*, 47-60.
2. R. O'hayre, S.-W. Cha, W. G. Colella, F. B. Prinz, *Fuel Cell Fundamentals*, 3rd edition, John Wiley & Sons, Inc., **2016**.
3. S. Choi, S. Yoo, J. Kim, S. Park, A. Jun, S. Sengodan, J. Kim, J. Shin, H. Y. Jeong, Y. Choi, G. Kim, and M. Liu, *Sci. Rep.* **2013**, *3*, 2426.
4. A. Sinha, D. N. Miller, and J. T. S Irvine, *J. Mater. Chem. A* **2016**, *4*, 11117-11123.
5. J. Kim, S. Choi, A. Jun, H. Y. Jeong, J. Shin, and G. Kim, *ChemSusChem* **2014**, *7*, 1669-1675.
6. R. Bove, S. Ubertini, *Modeling Solid State Fuel Cells: Chapter 2. Thermodynamics of Fuel Cell*, Springer, **2008**.
7. C. M. A. Brett, A. M. O. Brett, *Electrochemistry: Principles, Methods, and Applications*, Oxford University Press Inc., New York, **1993**.
8. C. K. Dyer, P. T. Moseley, Z. Ogumi, D. A. J. Rand, B. Scrosati, *Newnes, Encyclopedia of Electrochemical Power Sources* **2013**.
9. S. B. Adler, *Chem. Rev.* **2004**, 104, 4791-4843.
10. A. J. Jacobson, *Chem. Mater.* **2010**, *22*, 660-674.
11. M. A. Pena, J. L. G. Fierro, *Chem. Rev.* **2001**, *101*, 1981-2017.
12. K. Zhang, J. Sunarso, Z. Shao, W. Zhou, C. Sun, S. Wang, and S. Liu, *RSC Adv.* **2011**, *1*, 1661-1676
13. Z. Shao, S. M. Haile, *Nature* **2004**, *431*, 170-173.
14. Q. L. Liu, K. A. Khor, S. H. Chan, *J. Power Sources* **2006**, *161*, 123-128.
15. W. G. Wang, M. Mogensen, *Solid State Ionics* **2005**, *176*, 457-462.
16. C. Xia, W. Rauch, F. Chen, M. Liu, *Solid State Ionics* **2002**, *149*, 11-19.
17. A. A. Taskin, A. N. Lavrov, Y. Ando, *Prog. Solid State Chem.* **2007**, *35*, 481-490.
18. S. Choi, S. Park, J. Kim, T.-H. Lim, J. Shin, G. Kim, *Electrochem. Commun.* **2013**, *34*, 5-8.
19. G. Kim, S. Wang, A. J. Jacobson, L. Reimus, P. Brodersen, and C. A. Mims, *J. Mater. Chem.* **2007**, *17*, 2500-2505.
20. S. Yoo, A. Jun, Y.-W. Ju, D. Odkhuu, J. Hyodo, H. Y. Jeong, N. Park, J. Shin, T. Ishihara, and G. Kim, *Angew. Chem. Int. Ed*. **2014**, *53*, 13064-13067.
21. A. Jun, J. Kim, J. Shin, G. Kim, *Int. J. Hydrogen Energy* **2012**, *37*, 18381-18388.
22. J.-H. Kim, F. Prado, and A. Manthiram, *J. Electrochem. Soc.* **2008**, *155*, B1023-B1028.
23. J. M. Vohs, and R. J. Gorte, *Adv. Mater.* **2009**, *21*, 943-956.
24. Z. Jiang, C. Xia, F. Chen, *Electrochim. Acta* **2010**, *55*, 3595-3605.
25. D. Ding, X. Li, S. Y. Lai, K. Gerdes, and M. Liu, *Energy & Environ. Sci.* **2014**, *7*, 552-575.

Chapter 2. A Nano-structured SOFC Composite Cathode Prepared via Infiltration of $La_{0.5}Ba_{0.25}Sr_{0.25}Co_{0.8}Fe_{0.2}O_{3-\delta}$ into $La_{0.9}Sr_{0.1}Ga_{0.8}Mg_{0.2}O_{3-\delta}$ for Extended Triple-Phase Boundary Area

Reprinted with permission from J. Electrochem. Soc., 166, F805-F809 (2019). Copyright 2019, The Electrochemical Society.

2.1 Introduction

The worldwide global warming issues and limited fossil fuel supplies have been urging to develop next-generation renewable energy technologies.[1–3] Solid oxide fuel cells (SOFCs) have received great attention as promising energy devices with key benefits of low pollutant emissions, high energy conversion efficiency, and excellent fuel flexibility. Despite these attractive advantages, the high operating temperature of conventional SOFCs (800–1000°C) causes commercialization challenges including thermal stress between cell component, cost issues, and material compatibility problems. To make this device commercially feasible, the operating temperature should be further reduced down to an intermediate temperature range (500–700°C).[4–8]

Unfortunately, electrochemical performance is significantly deteriorated as the operating temperature is reduced, particularly due to the high polarization resistance (R_p) at the cathode. This implies that the development of electro-catalytically active cathode materials is imperative for sufficient oxygen reduction reaction (ORR) activities at lower operating temperatures. In this regard, mixed ionic and electronic conductors (MIECs), showing both electronically and ionically conductive properties, have been widely used as cathode materials. The MIECs could extend the reaction sites for ORR not only at the triple phase boundary (TPB) where the electronic conductor, ionic conductor, and gas meet simultaneously but also on the whole surface of MIECs, providing significantly improved SOFC performances.[9,10]

To further reduce the cathode R_p, an effective approach is to fabricate a composite configuration with cathode and electrolyte material for increasing electronic and ionic conduction path.[11] Typically, a conventional composite fabrication process (Figure 2.1(a)) requires high-temperature sintering step by mixing with cathode and electrolyte powders.[12] Such a high sintering temperature causes undesired interfacial reactions between the cathode and electrolyte material in the composite mixture, thereby limiting the materials selection and processing conditions. In order to avoid these difficulties, an infiltration method (Figure 2.1(b)) could be an alternative process for composite cathode fabrication. This method allows reducing the sintering temperature for composite cathode fabrication, unlike conventional composite fabrication process, since the cathode sintering process is separated from that

of the electrolyte. The lower sintering temperature further enables to improve electrochemical performance by maximizing the electrochemically reactive sites via nano-structured electrodes. Another strong point is associated with improved long-term stability based on reduced thermal expansion coefficient (TEC) mismatch between the cathode and electrolyte.[13–17] Generally, cobalt-based perovskite cathode materials suffer from high TEC issues in spite of their excellent electrical and catalytic properties. The TEC mismatch between the electrolyte and cobalt-based cathodes accelerates thermo-mechanical stresses at the interfaces during the heating or cooling process, which may lead to performance degradation. In this respect, the infiltration method effectively reduces this TEC mismatch by reason of electrolyte-based porous backbone.[15]

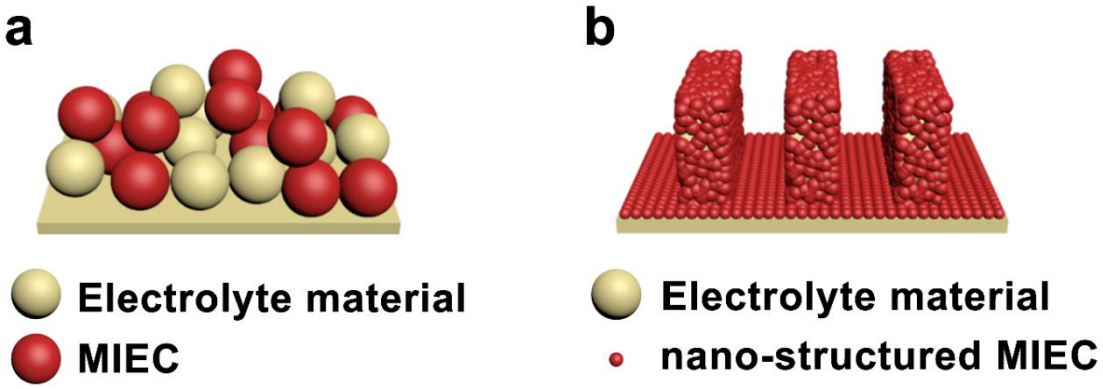

Figure 2.1. Schematic illustration of (a) a conventional composite electrode composed of MIEC and an electrolyte material (b) a composite electrode prepared by infiltration method.

These excellent advantages motivated us to employ the infiltration method for composite cathode fabrication with the cobalt-based perovskite materials in this study. A highly active $La_{0.5}Ba_{0.25}Sr_{0.25}Co_{0.8}Fe_{0.2}O_{3-\delta}$ (LBSCF) cathode is selected as a promising MIEC material due to its high oxygen ion diffusivity and high ORR catalytic activity at intermediate temperatures.[4,18,19] For electrolyte material selection, an yttria-stabilized zirconia (YSZ) electrolyte is widely used as the most reliable ionic-conducting material in SOFCs. However, the ionic conductivity is unacceptably low in an intermediate temperature range. Alternatively, a $La_{0.9}Sr_{0.1}Ga_{0.8}Mg_{0.2}O_{3-\delta}$ (LSGM) electrolyte is suggested as a promising electrolyte for IT-SOFCs on the basis of the high oxide ionic conductivity and good chemical stability in comparison with YSZ.[20,21] Here, we evaluate the microstructural, TEC, and electrochemical properties of the successfully fabricated nano-structured LBSCF-LSGM composite via infiltration method as an IT-SOFC cathode.

2.2 Experimental

The tape-casting method was used to fabricate the tri-layer cell (porous LSGM/ dense LSGM/ porous LSGM). To make dense LSGM layer, LSGM powder (Kceracell Co., Ltd) and brown menhaden fish oil (Tape casting warehouse) were put into an organic solution composed of ethanol and xylene (Aldrich, 98.5 + %). After ballmilling for 24 hours, polyalkylene glycol (Tape casting warehouse), butyl benzyl phthalate (Tape casting warehouse), and polyvinyl butyral (Tape casting warehouse) were added and then ball-milled for 24 hours again. To make porous LSGM layer, graphite as a pore former was added along with LSGM powder, and same fabrication procedures as dense LSGM slurry were conducted. The dense and porous LSGM slurries were fabricated into a shape of tape and then dried at room temperature. Resulting tapes were laminated as a tri-layer configuration and were fired at 1500°C for 6 hours in air. The thickness of the dense electrolyte layer and the porous electrode layer after firing is approximately 100 μm and 30 μm, respectively. The active electrode area is 0.36 cm^2. The porosity of porous LSGM scaffold measured by Archimedes method is about 60%.

To prepare the LBSCF solution, stoichiometric amounts of $La(NO_3)_3 \cdot 6H_2O$ (Aldrich, 99.9%), $Ba(NO_3)_2$ (Aldrich, 99+%), $Sr(NO_3)_2$ (Aldrich, 99+%), $Co(NO_3)_2 \cdot 6H_2O$ (Aldrich, 98+%), $Fe(NO_3)_3 \cdot 9H_2O$ (Aldrich, 98%), and citric acid were dissolved into distilled water. The pH value of the solution was adjusted to be approximately 4 by adding ammonium hydroxide. For an anode electrode, the $PrBaMn_2O_{5+\delta}$ (PBMO) solution was also prepared by the same abovementioned process using $Pr(NO_3)_3 \cdot 6H_2O$ (Aldrich, 99+%), $Ba(NO_3)_2$ (Aldrich, 99+%), $Mn(NO_3)_2 \cdot 4H_2O$ (Aldrich, 98%) and citric acid. For the single cell fabrication, LBSCF and PBMO solution were infiltrated into each porous LSGM scaffold at room temperature in ambient air. And then, the cells were calcined at 450°C in atmospheric pressure air. The infiltration process was repeated until 40 wt% loading amounts,[22–24] and the infiltrated cell was sintered at 800°C for 4 hours in air to form the desired perovskite structure.

The phase structure of materials was identified by X-ray diffraction (XRD) (Bruker D8 Advance) measurements in a range of $20^o < 2\theta < 60^o$. The microstructures of the LSGM and LBSCF were analyzed by using a scanning electron microscope (SEM) (Nova SEM).

To measure the electrochemical performance of an as-prepared cell, Ag paste was painted on the active electrode as a current collector and then Ag wires were attached to both electrodes. Then, the cell was laid on an alumina tube and fixed by a ceramic adhesive (Aremco, Ceramabond 552). AC impedance spectroscopy was used to evaluate the ASR of symmetric cells at open-circuit voltage (OCV) in air. For the single cell test, a flow rate of 100 mL min^{-1} of humidified H_2 (3% H_2O) and dry air were supplied to the anode and the cathode, respectively. I-V curves were obtained with a BioLogic Potentiostat in the temperature range from 550 to 700°C.

2.3 Results and Discussions

Figure 2.2(a) shows the XRD patterns of infiltrated LBSCF-LSGM composite sintered at 800°C in air. In general, undesired reactions at the interface between the electrode and the electrolyte materials in the composite mixture cause resistive secondary phases.[6] Such secondary phases degrade cell performance because they affect a restriction of electronic and oxide-ionic transport. Therefore, the composite should retain its own phases of the electrode and electrolyte materials at the sintering temperature. In terms of this reactivity screening, LBSCF- LSGM composite seems to be chemically compatible without any detectable impurities. Figure 2.2(b) presents the in-situ XRD patterns of LBSCF-LSGM composite prepared via infiltration method. LBSCF clearly maintains a simple perovskite structure over the measured temperature range without any undesirable reaction with LSGM. The main diffraction peaks of LBSCF shift to lower 2θ values with an increase of temperature, meaning that the volume of unit cell increases. Figure 2.2(c) displays the temperature dependence of the unit cell volume for LBSCF. The TEC was calculated by lattice volume change from the in-situ XRD patterns. The TEC value of infiltrated LBSCF is 16.6×10^{-6} K^{-1} in the temperature range of 100–800°C. Considering the TEC value of LSGM (11.5×10^{-6} K^{-1})[25] and general cobalt-based perovskite materials such as $GdBa_{0.5}Sr_{0.5}Co_{1.5}Fe_{0.5}O_{5+\delta}$ (24.0×10^{-6} K^{-1}),[26] it is confirmed that the infiltrated LBSCF exhibits a fairly acceptable TEC value.

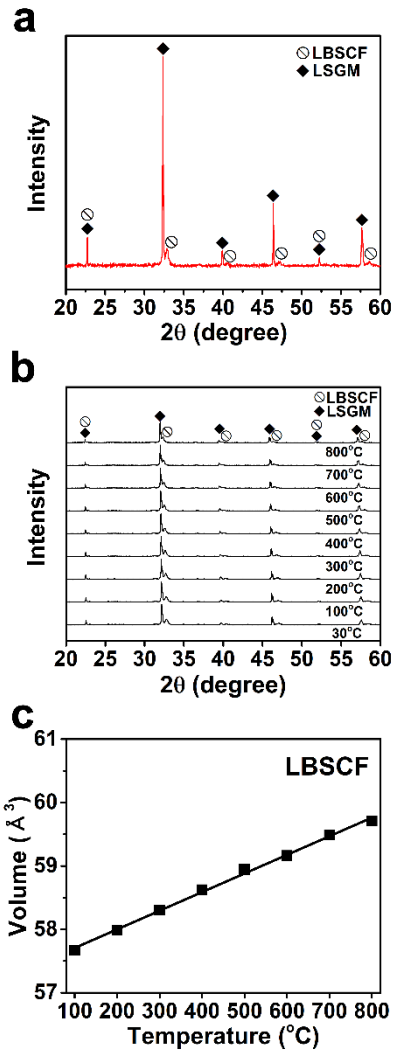

Figure 2.2. (a) XRD patterns of infiltrated LBSCF-LSGM composite sintered at 800ºC in air. (b) In-situ XRD patterns of infiltrated LBSCF-LSGM composite measured at various temperatures in air. (c) Temperature dependences of unit cell volume for LBSCF prepared by infiltration method.

Figure 2.3 presents a cross-sectional view of the tri-layer structure (porous LSGM/dense LSGM/porous LSGM) and high-resolution images of a porous LSGM before and after infiltration. Tri-layer structure of an as-prepared LSGM cell shows a well-made dense electrolyte layer without any observable pinholes or cracks and good adhesion between the electrolyte and electrode, as can be seen in Figure 2.3(a). The thickness of the electrolyte layer and the electrode layer is about 100 μm and 30 μm, respectively. Figures 2.3(b–d) indicate a porous LSGM scaffold before and after LBSCF infiltration. The fully-formed LBSCF nanoparticles are uniformly distributed with the average particle size of 30 nm on the surface of the LSGM. The uniform coating of nanoparticles could well create a good interconnection between the particles and thus improves ORR catalytic activity. Hence, nano-sized particles provide sufficient TPB length and high surface area for electrochemical reaction,

leading to outstanding electrochemical performance.[5,27–30] In these regards, the microstructure of infiltrated LBSCF-LSGM composite could be a key factor for excellent cell performance.

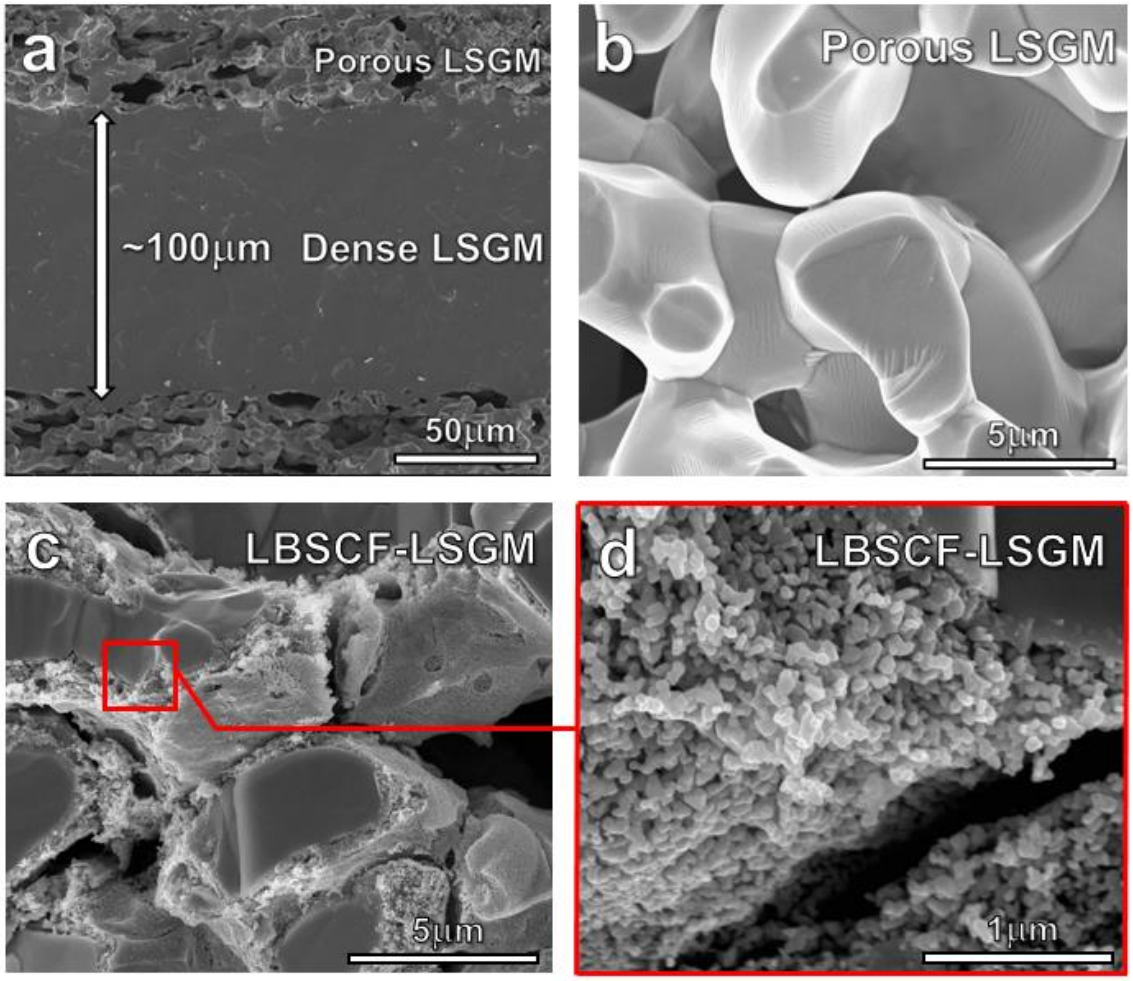

Figure 2.3. SEM images of (a) cross-sectional view of an as-prepared LSGM cell, (b) porous LSGM scaffold, (c) infiltrated LBSCF-LSGM composite sintered at 800°C in air, (d) high-resolution image of infiltrated LBSCF-LSGM composite.

Figures 2.4(a–c) show AC impedance spectra with fitting curve by equivalent circuit, Arrhenius plot, and short-term stability of a symmetric cell (LBSCF-LSGM/LSGM/LBSCF-LSGM). In the Nyquist plot of Figure 2.4(a), the ohmic resistance is the intercept of the real axis at high frequency and mainly comes from electrolyte resistance. Polarization resistance is a difference between high-frequency and low-frequency intercept in the real axis, which typically consists of a charge transfer resistance and a non-charge transfer resistance. The charge transfer resistance is mainly related to a charge transfer reaction during oxygen ion diffusion at the electrode and the non-charge transfer resistance is associated with oxygen surface exchange and gas-diffusion of the electrode surface.[31] The polarization resistances of infiltrated LBSCF-LSGM composite are 0.010, 0.020, and 0.049 Ω cm^2 at 700, 650, and

600°C, respectively, as shown in Figure 2.4(a). The results are extremely lower than those of conventional composite structured $La_{0.6}Sr_{0.4}Co_{0.2}Fe_{0.8}O_{3-\delta}$–LSGM (0.69 Ω cm^2 @ 600ºC)[32], infiltrated $Pr_2NiO_{4+\delta}$–LSGM (0.11 Ω cm^2 @ 650ºC)[33], infiltrated $SrFe_{0.75}Mo_{0.25}O_{3-\delta}$–LSGM (0.28 Ω cm^2 @ 600ºC)[34], and infiltrated $La_{0.5}Ba_{0.5}CoO_{3-\delta}$–LSGM (0.22 Ω cm^2 @ 600ºC)[35]. These exceptionally high electrochemical performances might be attributable to the extended TPB sites in relation to the LBSCF-LSGM microstructure shown in Figure 2.3 as well as high ORR catalytic activity of LBSCF. The impedance spectra data were fitted using an equivalent circuit consisting of ohmic resistance (R_1), and two parallel RQ elements (R_2Q_2-R_3Q_3) connecting in series as shown in the inset of Figure 2.4(a). A raw impedance spectra and the corresponding fit curves are in good agreement. The variation of the polarization resistance as a function of temperature in air is provided in Figure 2.4(b). The apparent activation energy values of LBSCF-LSGM composite from high-frequency (R_2) and low-frequency (R_3) arc contribution are 113.14 and 134.84 kJ mol^{-1} over the measured temperature range, respectively. In order to examine the composite stability in operating conditions, moreover, the ASRs of a symmetric cell were periodically measured at 600°C under OCV condition. As can be seen in Figure 2.4(c), the cell shows a fairly stable performance without any detectable degradation for 50 h.

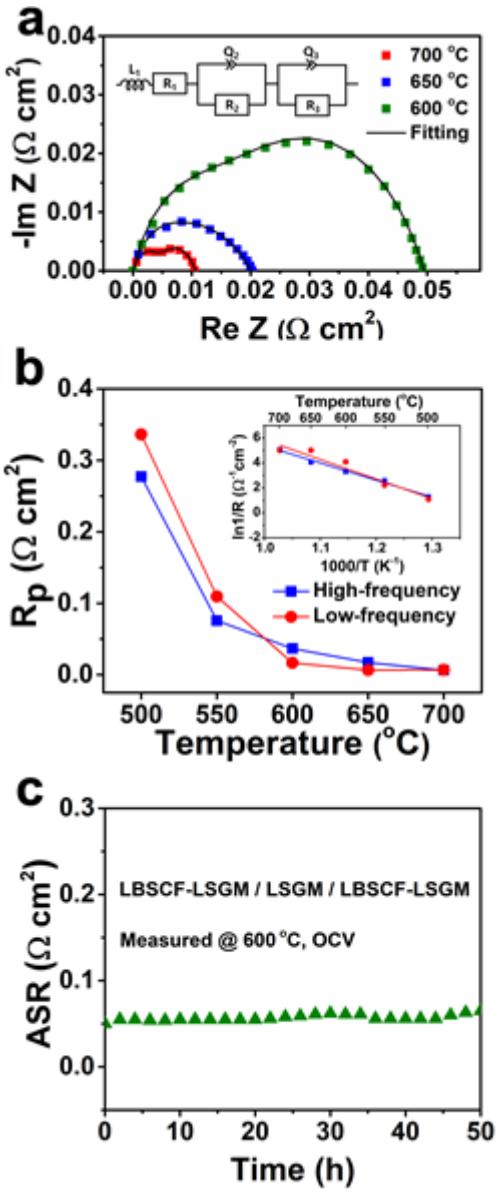

Figure 2.4. (a) Impedance spectra and (b) Polarization resistance as a function of temperature of a symmetric cell in air. The inset shows an Arrhenius plot of the polarization resistance from high-frequency and low-frequency arc contribution of a symmetric cell. (c) Short-term stability of a symmetric cell at 600ºC under OCV condition.

These results motivated us to select LBSCF as a cathode material for single cell fabrication. Moreover, PBMO is used for an anode material on the basis of its fast oxygen kinetics, good thermal stability, and high electrical conductivity in reducing condition.[36–40] An LSGM electrolyte-supported single cell (LBSCF- LSGM/LSGM/PBMO-LSGM) was prepared by LBSCF-LSGM composite cathode and PBMO-LSGM composite anode via infiltration method. Figure 2.5(a) presents the voltage and power density as a function of the current density for the single cell using humidified H_2 (3% H_2O) as the fuel

and dry air as the oxidant. The OCV values of a single cell are near 1.1 V in the measured temperature range, indicating a gastight sealing across the electrolyte. The maximum power densities are 0.902, 0.557, 0.303, and 0.133 W cm^{-2} at 700, 650, 600, and 550°C, respectively. To the best our knowledge, there is only one publication related to the single cell performance of LSGM-based infiltrated composite cathode. The maximum power density with infiltrated $Sr_2Fe_{1.5}Mo_{0.5}O_6$-LSGM composite cathode is demonstrated as 0.880 W cm^{-2} at 700°C which is similar to our study.[41] These performances are generally higher than YSZ-based infiltrated composite cathodes such as $GdBa_{0.5}Sr_{0.5}CoFeO_{5+\delta}$-YSZ (0.593 W cm^{-2} @ 700°C)[5] and $La_{0.6}Sr_{0.4}Co_{0.2}Fe_{0.8}O_{3-\delta}$-YSZ (0.640 W cm^{-2} @ 700°C)[42] because of high ionic conductivity of LSGM in an intermediate temperature range. The reasons for our high cell performance may be attributable to the microstructural benefits of the electrode, which expands electrochemically reactive sites. In addition, good electrocatalytic activity of LBSCF, and high ionic conductivity of LSGM had a positive effect on achieving high performance. Figure 2.5(b) shows the impedance spectra of a single cell under OCV condition. The ohmic resistances are 0.195, 0.288, 0.452, and 0.772 Ω cm^2 at 700, 650, 600, and 550°C, respectively. The non-ohmic resistances are 0.223, 0.320, 0.575, and 1.548 Ω cm^2 at 700, 650, 600, and 550°C, respectively. Considering extremely small cathode ASR, these non-ohmic resistances seem to be mainly originated from anodic losses.[13] The expected anodic polarization resistances are about 0.213, 0.300, 0.526, and 1.366 Ω cm^2 at 700, 650, 600, and 550°C, respectively. Therefore, the infiltrated LBSCF-LSGM composite could be an attractive cathode material for IT-SOFCs.

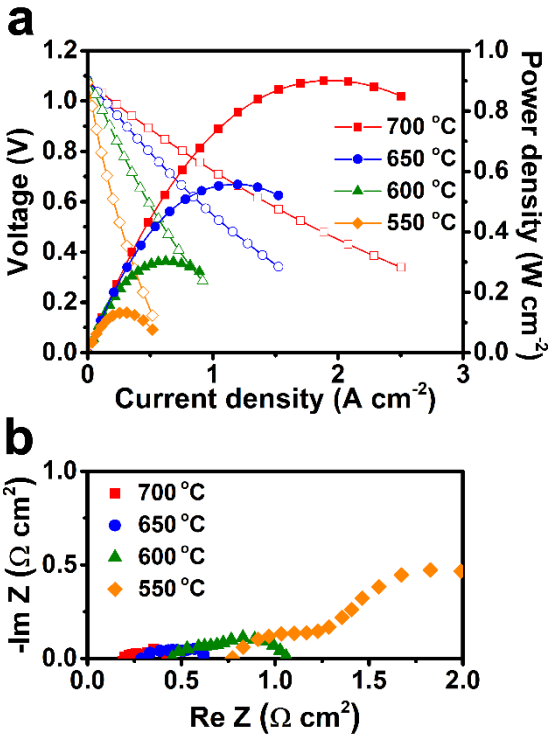

Figure 2.5. (a) I-V curves and corresponding power density curves and (b) impedance spectra of a single cell in a temperature range of 550-700ºC.

2.4 Conclusions

In summary, the composite with a highly active LBSCF cathode material and an LSGM electrolyte material was fabricated via infiltration method to maximize cathode performance from extended ORR reaction sites. The infiltrated LBSCF-LSGM composite cathode is evaluated in terms of microstructural, thermal expansion, and electrochemical properties for IT-SOFCs. Due to the relatively low sintering temperature for composite fabrication, nano-sized LBSCF- LSGM composite cathode is successfully formed. Moreover, the thermal expansion behavior of infiltrated LBSCF cathode is quite compatible with LSGM electrolyte. The ASR values of a symmetric cell with infiltrated LBSCF-LSGM composite are 0.010, 0.020, and 0.049 Ω cm^2 at 700, 650, and 600°C, respectively, and the maximum power density of a single cell is about 0.9 W cm^{-2} at 700°C. The present work demonstrates that infiltrated LBSCF-LSGM composite is considered to be a highly promising cathode material for IT-SOFCs.

References

1. M. S. Dresselhaus and I. L. Thomas, *Nature*, **414**, 332 (2001).
2. J. Brouwer, *Curr. Appl. Phys.*, **10**, S9 (2010).
3. C. Kim, J. Kim, S. Joo, Y. Bu, M. Liu, J. Cho, and G. Kim, *iScience*, **9**, 278 (2018).
4. J. Kim, S. Choi, A. Jun, H. Y. Jeong, J. Shin, and G. Kim, *ChemSusChem*, **7**, 1669 (2014).
5. S. Kim, A. Jun, O. Kwon, J. Kim, S. Yoo, H. Y. Jeong, J. Shin, and G. Kim, *ChemsusChem*, **8**, 3153 (2015).
6. S. Park, S. Choi, J. Shin, and G. Kim, *RSC Adv.*, **4**, 1775 (2014).
7. S. Choi, S. Yoo, J. Kim, S. Park, A. Jun, S. Sengodan, J. Kim, J. Shin, H. Y. Jeong, Y. Choi, G. Kim, and M. Liu, *Sci. Rep.*, **3**, 2426 (2013).
8. S. Joo, J. Kim, J. Shin, T.-H. Lim, and G. Kim, *J. Electrochem. Soc.*, **163**, F1489 (2016).
9. R. J. Gorte and J. M. Vohs, *Annu. Rev. Chem. Biomol. Eng.*, **2**, 9 (2011).
10. F. Bidrawn, R. Küngas, J. M. Vohs, and R. J. Gorte, *J. Electrochem. Soc.*, **158**, B514 (2011).
11. B. C. H. Steele, K. M. Hori, and S. Uchino, *Solid State Ionics*, **135**, 445 (2000).
12. Y. Choi, S. Choi, H. Y. Jeong, M. Liu, B. S. Kim, and G. Kim, *ACS Appl. Mater. Interfaces*, **6**, 17352 (2014).
13. J. M. Vohs and R. J. Gorte, *Adv. Mater.*, **21**, 943 (2009).
14. D. Ding, X. Li, S. Y. Lai, K. Gerdes, and M. Liu, *Energy Environ. Sci.*, **7**, 552 (2014).
15. Z. Jiang, C. Xia, and F. Chen, *Electrochim. Acta*, **55**, 3595 (2010).
16. Y. Cheng, A. S. Yu, X. Li, T.-S. Oh, J. M. Vohs, and R. J. Gorte, *J. Electrochem. Soc.*, **163**, F54 (2016).
17. G. Kim, J. M. Vohs, and R. J. Gorte, *J. Mater. Chem.*, **18**, 2386 (2008).
18. M. Li, B. Hua, J. Chen, Y. Zhong, and J. L. Luo, *Nano Energy*, **57**, 186 (2019).
19. A. J. Darbandi and H. Hahn, *Solid State Ionics*, **180**, 1379 (2009).
20. M. Li, Y. Zhang, M. An, Z. Lü, X. Huang, J. Xiao, B. Wei, X. Zhu, and W. Su, *J. Power Sources*, **218**, 233 (2012).
21. T. Ishihara, H. Matsuda, and Y. Takita, *J. Am. Chem. Soc.*, **116**, 3801 (1994).
22. Y. Huang, J. M. Vohs, and R. J. Gorte, *J. Electrochem. Soc.*, **152**, A1347 (2005).
23. H. He, Y. Huang, J. Regal, M. Boaro, J. M. Vohs, and R. J. Gorte, *J. Am. Ceram. Soc.*, **87**, 331 (2004).
24. M. F. Han, Z. Liu, and J. Qian, *ECS Trans.*, **35**(1), 2295 (2011).
25. J. Xue, Y. Shen, Q. Zhou, T. He, and Y. Han, *Int. J. Hydrogen Energy*, **35**, 294 (2010).
26. C. Kuroda, K. Zheng, and K. Swierczek, *Int. J. Hydrogen Energy*, **38**, 1027 (2013).
27. S. Kim, S. Choi, A. Jun, J. Shin, and G. Kim, *J. Electrochem. Soc.*, **161**, F1468 (2014).

28. S. Choi, J. Shin, and G. Kim, *J. Power Sources*, **201**, 10 (2012).
29. F. Wang, D. Chen, and Z. Shao, *J. Power Sources*, **216**, 208 (2012).
30. R. Zeng and Y. Huang, *Int. J. Hydrogen Energy*, **42**, 7220 (2017).
31. S. B. Adler, J. A. Lane, and B. C. H. Steele, *J. Electrochem. Soc.*, **143**, 3554 (1996).
32. Y. Lin and S. A. Barnett, *Solid State Ionics*, **179**, 420 (2008).
33. J. G. Railsback, Z. Gao, and S. A. Barnett, *Solid State Ionics*, **274**, 134 (2015).
34. X. Meng, D. Han, H. Wu, J. Li, and Z. Zhan, *J. Power Sources*, **246**, 906 (2014).
35. C. Setevich, S. Larrondo, and F. Prado, *Ceram. Int.*, **44**, 16851 (2018).
36. S. Sengodan, S. Choi, A. Jun, T. H. Shin, Y.-W. Ju, H. Y. Jeong, J. Shin, J. T. S Irvine, and G. Kim, *Nat. Mater.*, **14**, 205 (2015).
37. O. Kwon, S. Sengodan, K. Kim, G. Kim, H. Y. Jeong, J. Shin, Y.-W. Ju, J. W. Han, and G. Kim, *Nat. Commun.*, **8**, 15967 (2017).
38. S. Joo, O. Kwon, K. Kim, S. Kim, H. Kim, J. Shin, H. Y. Jeong, S. Sengodan, J. W. Han, and G. Kim, *Nat. Commun.*, **10**, 697 (2019).
39. S. Choi, S. Sengodan, S. Park, Y.-W. Ju, J. Kim, J. Hyodo, H. Y. Jeong, T. Ishihara, J. Shin, and G. Kim, *J. Mater. Chem. A*, **4**, 1747 (2016).
40. M. Li, B. Hua, Y. Zeng, B. S. Amirkhiz, and J.-L. Luo, *J. Mater. Chem. A*, **6**, 15377 (2018).
41. J. Liu, Y. Lei, Y. Li, J. Gao, D. Han, W. Zhan, F. Huang, and S. Wang, *Electrochem. Commun.*, **78**, 6 (2017).
42. H. Fan, M. Keane, N. Li, D. Tang, P. Singh, and M. Han, *Int. J. Hydrogen Energy*, **39**, 14071 (2014).

List of Publications

1. **Seungtae Lee**, Seona Kim, Sihyuk Choi*, Jeeyoung Shin*, and Guntae Kim* "A Nano-Structured SOFC Composite Cathode Prepared via Infiltration of $La_{0.5}Ba_{0.25}Sr_{0.25}Co_{0.8}Fe_{0.2}O_{3-\delta}$ into $La_{0.9}Sr_{0.1}Ga_{0.8}Mg_{0.2}O_{3-\delta}$ for Extended Triple-Phase Boundary Area" ***J. Electrochem. Soc.***, 166 (2019) F805-F809.

2. Seona Kim, **Seungtae Lee**, Junyoung Kim, Jeeyoung Shin*, and Guntae Kim* "Self-Transforming Configuration Based on Atmospheric-Adaptive Materials for Solid Oxide Cells" ***Sci. Rep.***, 8 (2018) 17149.

Acknowledgements

I would like to express my deepest gratitude to all of the supporters who give encouragement and support for completing my master`s thesis. It would have been difficult to write this thesis without their help. So, I would like to take this opportunity to express my appreciation.

The driving force to complete this paper is the constant support of my advisor, Prof. Guntae Kim. He gave me endless support, enormous knowledge, encouragement with patience, and guidance for completing the thesis. I sincerely appreciate his support and will never forget his help.

I am also grateful to all of my committee members: Prof. Changhee Sohn, and Prof. Ikwhang Chang. Their expertise and insightful comments helped me to improve my knowledge.

I also appreciate Prof. Jeeyoung Shin and Prof. Sihyuk Choi. They always listened to my thoughts and shared their academic knowledge. It would have been impossible to complete the thesis without their support.

The following lab members gave me impressive memories and endless help: Prof. Yunfei Bu, Prof. Sivaprakash Sengodan, Prof. Young-Wan Ju, Dr. Arunchander Asokan, Dr. Areum Jun, Dr. Junyoung Kim, Dr. Ohhun Gwon, Dr. Seona Kim, Sangwook Joo, Chaehyun Lim, Ohhun Kwon, Changmin Kim, Donghwi Jeong, Jeongwon Kim, Gihyeon Kim, Hyojea Hwang, Hansol Lee, Arim Seong, and Yejin Yang. I wish all their work well.

Last but not least, I would like to sincerely thank my family for their endless support, love, and encouragement.